Experimental and Numerical Investigation of Rubber Damping Ring and Its Application in Multi-span Shafting

Haimin Zhu[1], Weifang Chen[1,*], Miaomiao Li[1], Rupeng Zhu[1], Li Zhang[2], Bibo Fu[3], Shuai Wang[3] Xiong Lu[3]

[1]National Key Laboratory of Science and Technology on Helicopter Transmission, Nanjing University of Aeronautics and Astronautics, Nanjing, 210016, China
[2]Faculty of Engineering and Environment, Northumbria University, Newcastle, NE1 8ST, UK
[3]AECC Hunan Aviation Powerplant Research Institute, Zhuzhou, 412000, China

* Corresponding author: Weifang Chen
Email: meewfchen@nuaa.edu.cn, Tel: +86 18252002433

Abstract A new approach for establishing the mechanical model of the rubber damping ring was studied numerically and experimentally. Firstly, parameters of Mooney-Rivlin and Prony series models of the rubber material were identified based on ISIGHT integrating with ANSYS and MATLAB, in which the rubber damping ring's hysteresis loop was obtained by vibration experiment and ANSYS simulation, respectively; meanwhile, the dynamic stiffness and damping were calculated simultaneously by a parameter separation and identification method. Subsequently, the accuracy of the constitutive model parameters was verified experimentally. In light of this, based on the experimental design and the approximate model method of the joint simulation platform, a mechanical model of dynamic stiffness and damping of the rubber damping ring was established. Finally, the rubber damping ring's mathematical model was employed to perform a vibration reduction analysis in a multi-span shafting, where the numerical and experimental investigation was conducted, respectively. The results show that the theoretical and experimental error of vibration reduction rate is less than 17%, which verify the accuracy of the mechanical model of the rubber damping ring.

Keywords Rubber damping ring; Hysteresis loop; Multi-span shafting; Vibration reduction

1 Introduction

The installation of a damping ring between the bearing and the support can significantly reduce the bending vibration of the transmission system. Rubber damping ring is widely employed in vibration and noise reduction of the rotor system due to its low cost and simple manufacturing process. It can be known that the dynamic performance of the rubber damping ring varies owing to factors such as rubber hardness, temperature, excitation frequency and excitation amplitude. Therefore, the establishment of an accurate mechanical model of the rubber damping ring is the prerequisite for achieving proper vibration reduction effects.

The rubber material is a typical viscoelastic substance. Researchers in the field have carried out substantial studies on rubber damping ring. Currently, the mechanical modelling methods of rubber damping ring mainly include theoretical, finite element and experimental modelling. For the theoretical modelling method, the earliest dynamic models to simulate rubber's dynamic

characteristics are the Maxwell model and Kelvin-Voigt model [1-2]; however, these models possess few parameters and cannot precisely depict the dynamic characteristics of the rubber damping ring. Therefore, the generalised Maxwell model, generalised Kelvin-Voigt model and the Zener model [3-5] have been proposed. The fundamental idea of these models is to employ multiple Maxwell models or various Kelvin-Voigt models in series or parallel [6-7]. Sjoberg et al. [8-9] employed a fractional derivative model to develop a mechanical model of the rubber element, which contains both an elastic element and a friction element. Berg et al. [10] proposed a smooth friction model, which is utilised to conduct dynamic behaviour analysis of the rotor-bearing system with rubber damping ring, and has been widely recognised and adopted in the field. Based on the nonlinear shape coefficient method, Hill et al. [11] calculated the static stiffness of the rubber damper theoretically; however, only the static stiffness of the rubber damper with regular shape can be calculated. Luo et al. [12] predicted the complete loading-unloading response utilising an energy dissipation method by means of modifying the classical hyperelastic model. A new approach in their work was proposed to simulate the dynamic impact characteristics of rubber and verified by experiments. Zhao et al. [13] studied a dynamic model of a nonlinear hysteretic vibration isolation system, which consists of nonlinear stiffness and nonlinear damping. Yu et al. [14] carried out a comparative investigation of parameter identification methods and prediction efficiency of Kelvin-Voigt, three-parameter Maxwell, Berg and Dzierzek models, and then analysed the characteristics and application scenarios of these four models. Additionally, based on a static stiffness mechanism, Zhao et al. [15] established a mechanical model through dynamic excitation experiments.

With the development of finite element modelling methods for viscoelastic materials, commonly accepted hyperelastic constitutive models include Mooney-Rivlin, Ogden, Neo-Hookean, Yeoh and Polynomial [16-17], which are mainly used to predict the nonlinear static stiffness of rubber components. The dynamic properties are associated with load amplitude, frequency, temperature and other factors when rubber components are utilised in the dynamic load environment. Currently, viscoelastic material models, such as generalised Maxwell and Prony series models, have been introduced into finite element analysis software to describe the effects of amplitude and frequency on the dynamic performance of rubber components. The parameters of the hyperelastic and viscoelastic constitutive models can be determined by making standard specimens and carrying out corresponding experiments [18-19]. Utilising finite element software, Charlton[20], Zielnica [21], and Negrete [22] implemented static and dynamic simulation analysis on the rubber damper to predict the static and dynamic stiffness of the damper. Rahnavard [23] and Sheikhi [24] studied the rubber modeling using ABAQUS and ANSYS. However, in some cases, standard specimens which test the properties of rubber materials cannot be obtained; therefore, the parameters of the constitutive model of rubber materials can only be identified by means of investigating the overall mechanical characteristics of rubber dampers. Liu et al. [25-26] investigated the dynamic characteristic analysis method of rubber damper, and then proposed an optimisation method to determine the parameters of the viscoelastic model of rubber materials by way of ISIGHT software integrating with ANSYS and MATLAB, and verified it experimentally.

The application of power and elliptic functions to fitting and identifying the hysteresis curve of the rubber damping ring is also a hot topic in recent years [27-28]. Sun et al. [29-30] conducted dynamic experiments on rubber damping rings, which generates the force and displacement curves at various frequencies and amplitudes. Subsequently, the parameters of the elastic and damping

forces were identified, and the relationship between the elastic coefficient and damping coefficient and frequency was achieved, respectively. Han et al. [31] trained the neural network using experimental data, and then utilised the least square surface to align with the output of the neural network; afterwards, the mechanical model of the dynamic stiffness and damping of the rubber damper was established. Based on the literature reviewed, there exist several mechanical modelling methods for rubber damping rings. However, there is a lack of concise and compelling research proposals due to insufficient understanding of the properties of rubber materials. Besides, the derivation process is complicated and cannot precisely depict the dynamic characteristics of the rubber damping ring. At the same time, the rubber damping ring's mathematical model was difficult to couple with the whole system. In this research, a mechanical model of a rubber damping ring is established by combining finite element and experimental modelling methods. Not only various constitutive model parameters of rubber materials are obtained easily, but also a simple and highly-efficient function of the rubber damping ring is developed, which can be conveniently coupled with the rotor system for dynamic analysis.

Firstly, according to the structure and loading condition of the rubber damping ring in the transmission shaft system, a test fixture is made. The hysteresis loops of the rubber damping ring under various excitation amplitudes and frequencies are achieved based on dynamic experiments. Then the dynamic stiffness and damping of the rubber damping ring under corresponding working conditions are obtained by way of a parameter separation and identification method. Subsequently, a joint simulation platform based on ISIGHT software is built, and utilizing the Radial Basis Approximation Function and Multi-Objective Particle Swarm Optimization (PSO), the hyperelastic and viscoelastic constitutive model parameters of the rubber materials are identified and verified experimentally. In light of this, based on the Optimal Latin Hypercube Design and Response Surface Approximation Function of co-simulation platform, the dynamic stiffness and damping of the rubber damping ring with various amplitudes and frequencies are analysed, and the mechanical model of dynamic stiffness and damping of rubber damping ring is constructed. Finally, the established mechanical model of the rubber damping ring is applied to multi-span shafting to investigate the vibration reduction performance and verify the precision of the mechanical model experimentally. This research lays a theoretical foundation for the design of a rubber damping ring in vibration and noise reduction of the shafting.

2 Experimental Studies on Dynamic Stiffness and Damping of Rubber Damping Ring

In this study, the rubber damping ring in a helicopter tail transmission shaft system is investigated, in which its shore hardness is 80. The schematic diagram of the helicopter tail transmission shaft system and rubber damping ring is shown in Fig. 1.

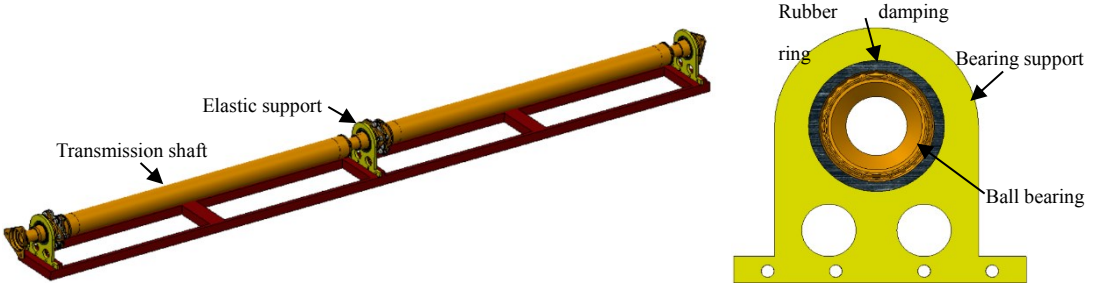

(a) Helicopter tail transmission shaft system (b) Rubber damping ring

Fig. 1 Schematic diagram of the helicopter tail transmission shaft system and rubber damping ring

2.1 Rubber damping ring test

According to the structure and loading condition of the rubber damping ring, the test fixture is designed, as shown in Fig. 2. The rubber damping ring's test fixture comprises an upper clamping, a lower clamping, a central shaft and a tightening nut. Subsequently, the dynamic characteristics of the rubber damping ring could be experimented and studied by the electro-hydraulic servo testing machine. The electro-hydraulic servo testing machine is exhibited in Fig. 3, which mainly contains a fixed chuck and a moving chuck. The lower clamping of the test fixture is clamped by the fixed chuck of the electro-hydraulic servo testing machine, and the moving chuck pulls the rubber damping ring to make sinusoidal displacement motion with various amplitudes and frequencies in the radial direction, as shown in Fig. 4.

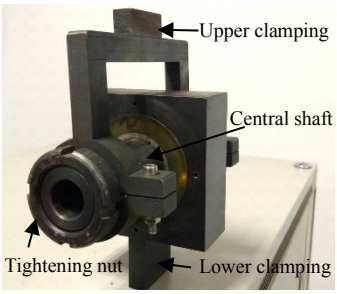

Fig. 2 Test fixture

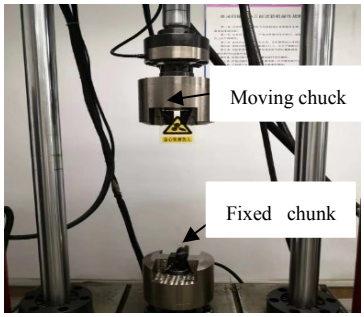

Fig. 3 Electro-hydraulic servo testing machine

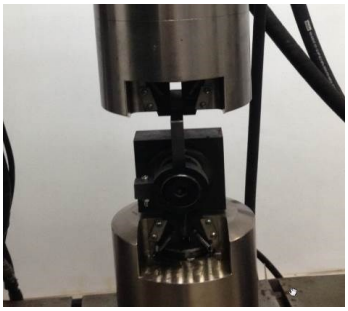

Fig. 4 Schematic view of the dynamic test

It exhibits a phase lag phenomenon when the rubber damping ring is under cyclic loading, and the force and displacement curves form a hysteresis loop. The area of the hysteresis loop is the energy dissipated by the rubber material in one cycle. Hysteresis loops of the rubber damping ring under various excitation frequencies and amplitudes are obtained utilising dynamic experiments. Figs. 5-6 manifest the dynamic characteristic curves of some particular test conditions. As shown in Fig. 5, under the identical excitation frequency, i.e. 4Hz, the inclination angle of the hysteresis loop is invariant basically with the increase of the excitation amplitude. The hysteresis loop's area increases with the escalation of amplitude. As displayed in Fig. 6, at the same excitation amplitude, i.e. 0.2mm, the hysteresis loop's inclination angle increases as the excitation frequency upsurges.

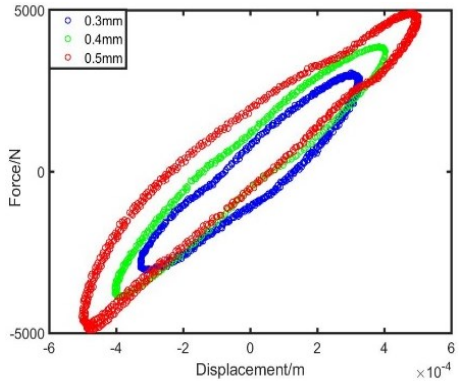

Fig. 5 Hysteresis loops with various amplitudes at frequency 4Hz

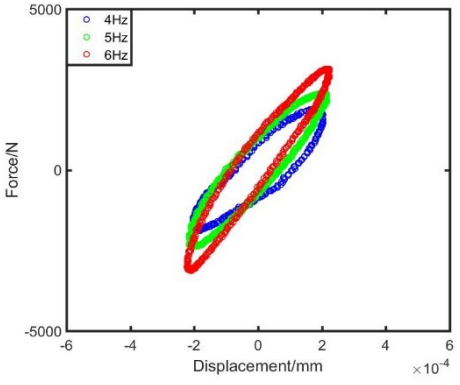

Fig. 6 Hysteresis loops with various frequencies at amplitude 0.2mm

2.2. Parameter separation and identification method

The hysteresis loop of the rubber damping ring is decomposed into both a power function curve and an elliptic function curve. Consequently, Load F is decomposed into elastic force F_k and viscous damping force F_c, i.e.,

$$F = F_k + F_c \tag{1}$$

The damping force can be expressed as an elliptic function centred on the origin, and the corresponding equation can be written as

$$\frac{X^2}{A^2} + \frac{F_c^2}{B^2} = 1 \tag{2}$$

where X is the vibration displacement; F_c denotes the damping force; A represents the amplitude of displacement excitation; B indicates the minor half axis of the ellipse.

Elliptic functions can also be presented as parametric equations, i.e.,

$$\mathrm{X} = \mathrm{A}\sin(2\pi f\mathrm{t}) \tag{3}$$

$$F_c = \mathrm{B}\cos(2\pi f\mathrm{t}) \tag{4}$$

Here f is the excitation frequency.

The damping force is equivalent to viscous damping force, while F_c is proportional to velocity, which can be obtained as follows.

$$F_c = \mathrm{C}(A,f)\dot{\mathrm{X}} = C(A,f)A\omega\cos(2\pi f\mathrm{t}) \tag{5}$$

where $\mathrm{C}(A,f)$ denotes the damping coefficient; $\dot{\mathrm{X}}$ represents the vibration speed; ω is the circular frequency.

Combining equations (4) and (5), the viscous damping coefficient can be calculated by

$$\mathrm{C}(A,f) = \frac{B}{A\omega} \tag{6}$$

The energy consumed by the system in one motion period equals to the area of the ellipse, and the formula is $\mathrm{S} = \pi\mathrm{AB}$. According to the test data, the energy consumed by the system in one cycle is $S_{loss} = \oint \mathrm{Fdx}$, then

$$\mathrm{B} = \frac{\oint \mathrm{Fdx}}{\pi A} \tag{7}$$

By taking equation (7) into equation (6) into account, the viscous damping coefficient can be rewritten as

$$\mathrm{C}(A,f) = \frac{\oint \mathrm{Fdx}}{\pi\mathrm{A}^2\omega} \tag{8}$$

The elastic force F_k can be given by

$$F_k = F - \frac{\oint \mathrm{Fdx}}{\pi\mathrm{A}}\cos(2\pi f\mathrm{t}) \tag{9}$$

The rubber damping ring's dynamic stiffness $K(A,f)$ can be represented as

$$K(A,f) = (F_{kmax} - F_{kmin})/(X_{max} - X_{min}) \tag{10}$$

where X_{max} and X_{min} represent the maximum and minimum vibration displacement boundaries in one motion period, respectively; F_{kmax} and F_{kmin} are the maximum and minimum elastic forces in a motion cycle, respectively

Hence, the hysteresis loop of the rubber damping ring can be decomposed into both an inclined straight line representing the elastic force and an ellipse standing for the viscous force by using the parameter separation and identification method. The elastic and the viscous forces, which are obtained by decomposing the hysteresis loop corresponding to different excitation frequencies and

amplitudes, are varied, as indicated in Fig. 7.

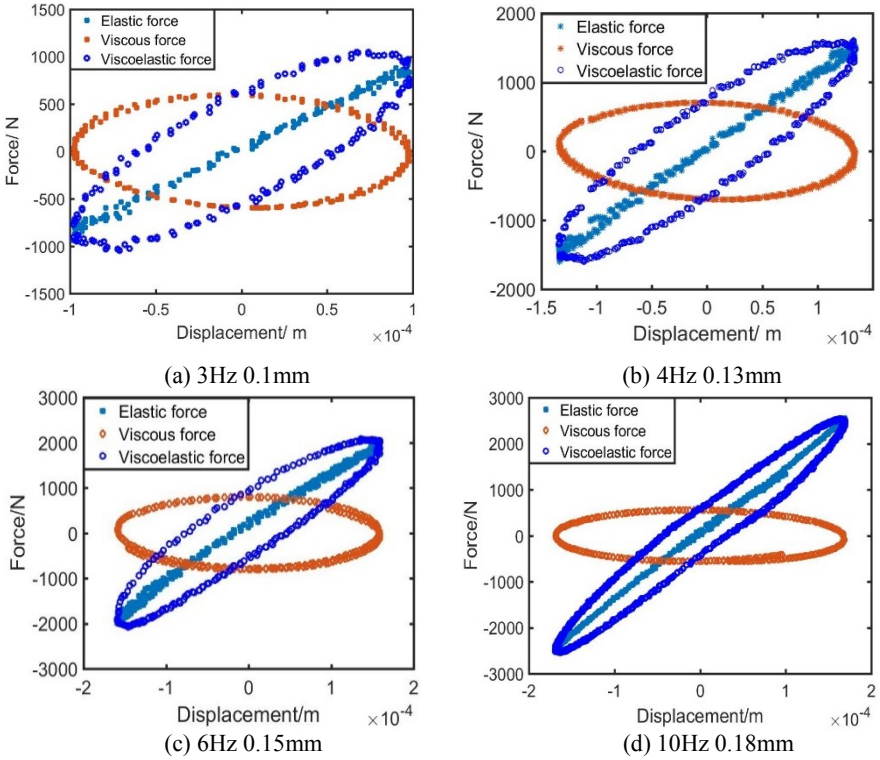

(a) 3Hz 0.1mm (b) 4Hz 0.13mm

(c) 6Hz 0.15mm (d) 10Hz 0.18mm

Fig. 7 Decomposition diagram of the hysteresis loop under various excitation frequencies and amplitudes

3. Parameter Identification of Constitutive Model of the Rubber Material

3.1. Simulation analysis of rubber damping ring based on ANSYS

Transient dynamic analysis of rubber damping ring is carried out in ANSYS software. The 3D model of a rubber damping ring is demonstrated in Fig. 8, which mainly consists of a rubber ring and metal bushing. The metal bushing is made of steel with a density of 7850kg/m^3, an elastic modulus of 2×10^{11}Pa and Poisson's ratio of 0.3. Rubber material's density is 1200kg/m^3, and Poisson's ratio is 0.495. The hyperelastic model employs a two-parameter Mooney-Rivlin model, in which the initial parameters are assigned as follows, i.e. $C_{10}=4.56\times10^6$, $C_{01}=-2.5\times10^5$, $d = (1-2\upsilon)/(C_{10}+C_{01})$; The Prony series model is used for the viscoelastic model, in which initial parameters are listed as follows, i.e. $\alpha_1=0.06$, $\alpha_2=0.02$, $\tau_1=0.55$ and $\tau_2=0.0008$. Binding contact is adopted between the metal bushing and the rubber ring; subsequently, Solid185 element is chosen, and the rubber damping ring is meshed by the sweeping command, with a total of 4012 nodes. A harmonic displacement load A=0.00015sin(6×2πt) is applied to the centre of the rubber damping ring, wherein the centre point is connected with the inner surface of the metal bushing by way of rigid beams. Meanwhile, fixed constraints are imposed on the outer surface of the rubber damping ring. The mesh model and constraints of the rubber damping ring are exhibited in Fig. 9. Finally, the result data are collected and exported.

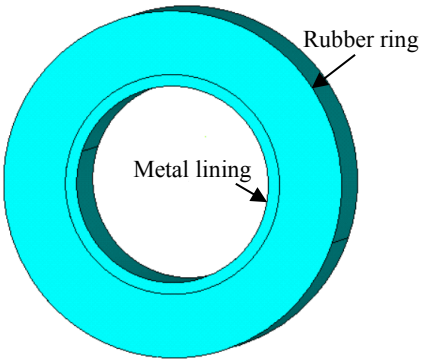

Fig. 8 3D model of the rubber damping ring

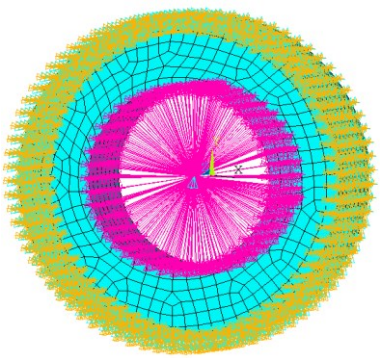

Fig. 9 Mesh model and constraints of the rubber damping ring

3.2. Data processing and analysis based on MATLAB

MATLAB is utilised to analyse the result data of ANSYS simulation, to obtain each coefficient of the elliptic equation by means of fitting the hysteresis loop with the least square method, thus achieving the long and short axes of the ellipse, as exhibited in Fig. 10. The hysteresis loop obtained by simulation is decomposed into both an inclined straight line denoting elastic force and an ellipse representing viscous force by employing the parameter separation and identification method, as presented in Fig. 11.

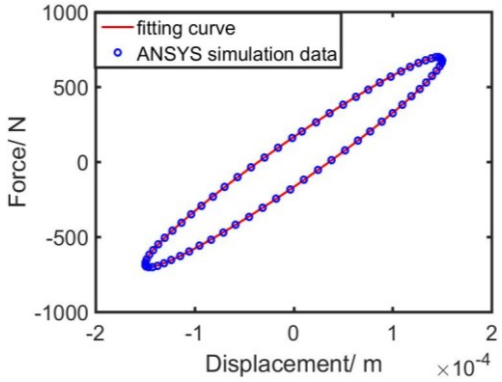

Fig. 10 Diagram of least square fitting with the elliptic equation

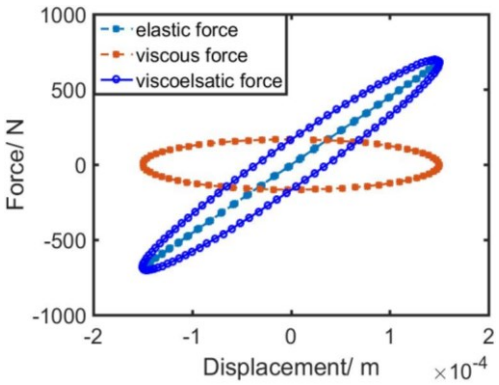

Fig. 11 Decomposition diagram of hysteresis loop obtained by simulation

3.3. Joint simulation based on ISIGHT

The hysteresis loops of the rubber damping ring under the working conditions of 6Hz and 0.15mm are calculated through the experiment and simulation, respectively. Subsequently, the dynamic stiffness and damping under the corresponding conditions can be achieved by the parameter separation and identification method. In order to automatically identify the constitutive model parameters of the rubber material in the rubber damping ring, the optimisation software ISIGHT integrates ANSYS and MATLAB to build a joint simulation platform. The specific process is exhibited in Fig. 12. The effect picture of ISIGHT integrated with ANSYS and MATLAB is manifested in Fig. 13.

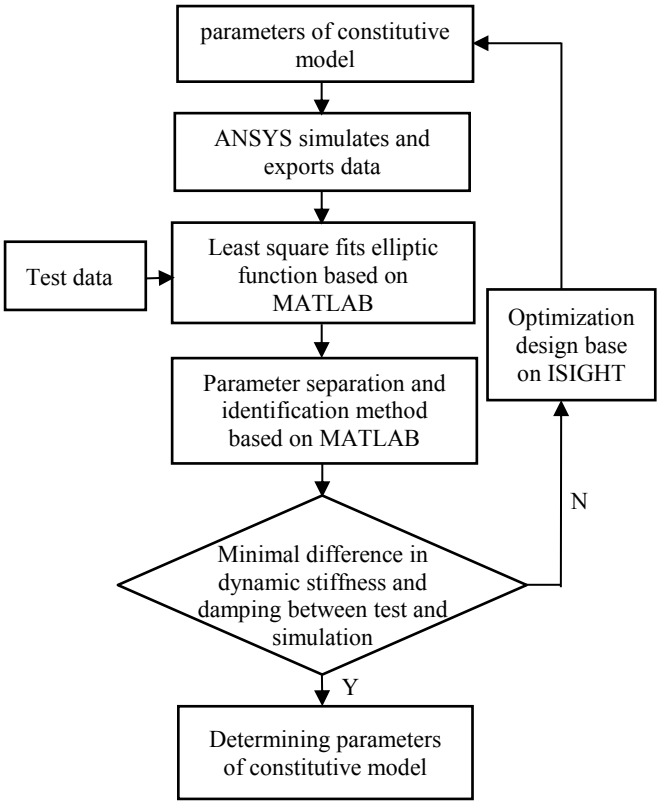

Fig. 12 Flow chart of parameters identification for the constitutive model of rubber damping ring material

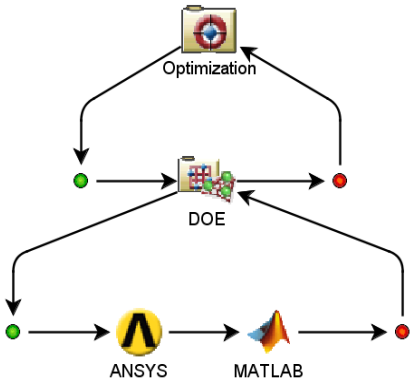

Fig. 13 Effect diagram of integration of ANSYS and MATLAB in ISIGHT

The hyperelastic and viscoelastic constitutive model parameters of the rubber material are used as design variables, and a sample space was constructed, as shown in Table 1. The Optimal Latin Hypercube Design is employed to generate test points in the sample space [32]. Then the dynamic stiffness and damping of the corresponding test points are obtained under the cooperative work of ANSYS and MATLAB.

Table 1 Constitutive model parameters of rubber material

Design variable	Initial value	Minimum value	Maximum value
C_{10}	4.56×10^{6}	2.4506×10^{5}	2.4506×10^{7}
C_{01}	-2.5×10^{5}	-9.6×10^{6}	-9.6×10^{4}
α_1	0.06	0	1
τ_1	0.55	0	1
α_2	0.02	0	1
τ_2	0.0008	0	1

As the transient dynamic analysis of the rubber damping ring is a time-consuming process, in order to improve the optimization efficiency, Radial Basis Approximation Function is employed to reflect the relationship between the dynamic stiffness, damping and the constitutive model parameters of the rubber material. The optimal value of constitutive model parameters of the rubber material is determined through multi-objective PSO algorithm, in which the minimal difference between dynamic stiffness and damping of experiment and simulation results is used as the objective function under the identical working condition, and the objective function F_o can be expressed as

$$\begin{cases} minF_o = min[f_1, f_2] \\ f_1 = |K_s - K_e| \\ f_2 = |C_s - C_e| \end{cases} \tag{11}$$

where K_s and K_e represent the rubber ring's dynamic stiffness obtained from simulation and experiment, respectively; C_s and C_e are the damping of the rubber ring solved from simulation and experiment, respectively.

Then, the joint simulation platform is executed, and finally, the optimal solution is obtained, specifically as manifested in Table 2.

Table 2 The identified optimal values of constitutive model parameters of rubber material

Constitutive model parameters	Optimal value
C_{10}	8.5×10^6
C_{01}	-4.62×10^5
α_1	0.1609
τ_1	0.10205
α_2	0.57
τ_2	0.0129

3.4. Test verification

Experiments were carried out on an electro-hydraulic servo testing machine so as to verify the accuracy of constitutive model parameters of the rubber material acquired by joint simulation. The hysteresis loops of the test and the simulation are plotted, respectively, as exhibited in Fig. 14. It can be observed that the hysteresis loops obtained by the test and simulation are in coincidence basically. Meanwhile, the comparative analysis of the dynamic stiffness and damping results obtained by test and simulation is displayed in Table 3, in which the maximum error rate is not more than 7%. In summary, the identification of constitutive model parameters of rubber material by way of ISIGHT integrating with ANSYS and MATLAB has high credibility and meets the needs of practical engineering.

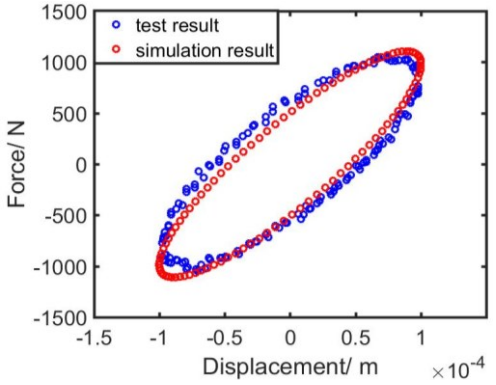

(a) 3Hz 0.1mm

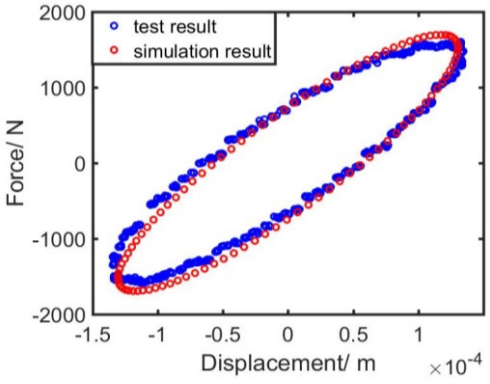

(b) 4Hz 0.13mm

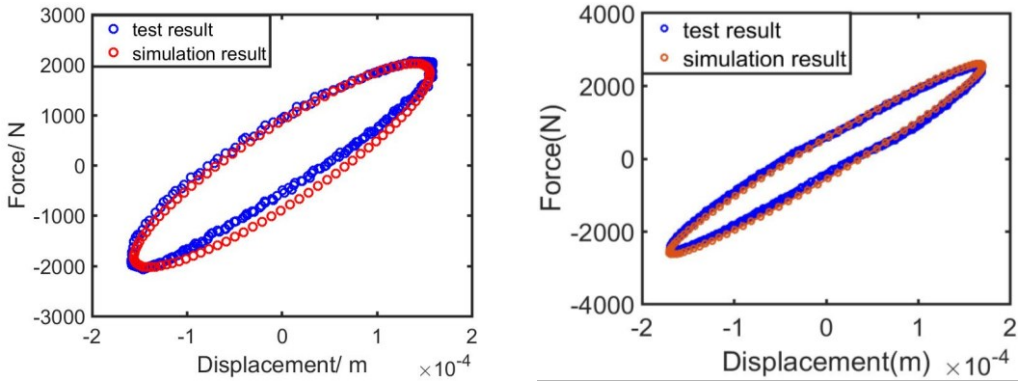

(c) 6Hz 0.15mm (d) 10Hz 0.18mm

Fig. 14 Simulation and test results of hysteresis loop analysis of rubber damping ring

Table 3 Comparative analysis of dynamic stiffness and damping between test and simulation

Frequency/ Hz	Amplitude/ mm	Simulation result		Test result		Error	
		Stiffness/ N/m	Damping/ N·s·m^{-1}	Stiffness/ N/m	Damping/ N·s·m^{-1}	Stiffness	Damping
3	0.1	11043497	242087	10964563	227087	4.3%	6.2%
4	0.13	11956146	200263	11140818	213270	6.8%	6.1%
6	0.15	13622507	163608	13097922	144859	3.8%	5.3%
10	0.18	16681722	111647	17136266	117880	2.7%	5.6%

4 Mechanical Modelling of the Dynamic Stiffness and Damping of Rubber Damping Ring

The constitutive model parameters of the rubber material are determined through the research studies above. In this section, the mechanical models of the dynamic stiffness and damping of the rubber damping ring under various excitation amplitudes and frequencies are investigated by means of simulation directly. Similarly, a joint simulation platform is built by integrating ISIGHT with ANSYS and MATLAB. The rubber damping ring's dynamic stiffness and damping in the corresponding working conditions are obtained by the experimental design method, in which the excitation amplitude and frequency are chosen as input variables. Finally, the Response Surface Function is employed to fit excitation and response to obtain approximate models of the relationship between the amplitude and frequency and the rubber damping ring's dynamic stiffness and damping, as exhibited in Fig. 15. The effect diagram of ISIGHT integrated with ANSYS and MATLAB is presented in Fig. 16.

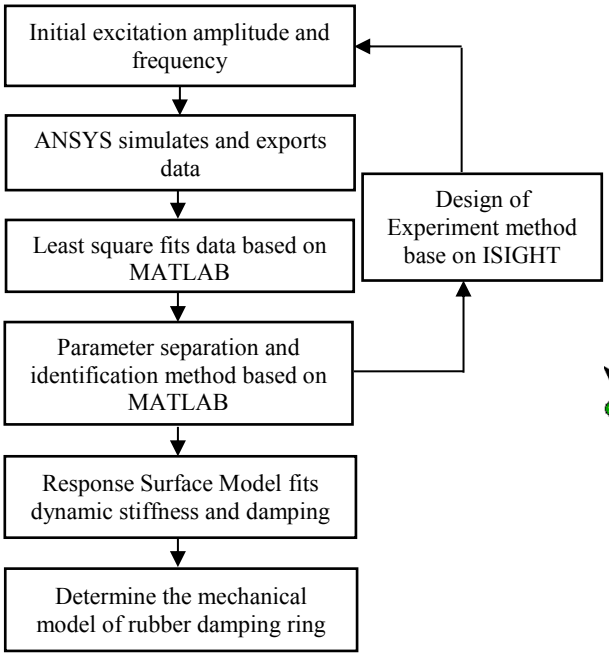

Fig. 15 Flow chart for the mechanical modelling of the rubber damping ring

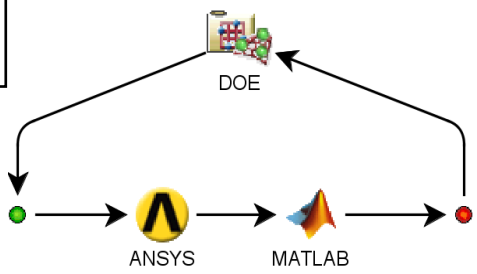

Fig. 16 Effect diagram of integrating ANSYS and MATLAB into ISIGHT

The range of excitation amplitude and frequency of the rubber damping ring is selected according to its actual operating conditions, as shown in Table 4.

Table 4 The range of excitation amplitude and frequency of the rubber damping ring

Input parameter	Initial value	Minimum	Maximum
Amplitude/m	0.0005	0.0001	0.0015
Frequency/Hz	10	2	80

The Optimal Latin Hypercube Design method is applied to generate test points in the sample space composed of excitation amplitude and frequency. The dynamic stiffness and damping of the corresponding test points are obtained by the joint simulation, and the specific values are given in Table 5.

Table 5 Test points and corresponding dynamic stiffness and damping

No.	Amplitude/m	Frequency/Hz	Dynamical stiffness/ N/m	Damping/ $N \cdot s \cdot m^{-1}$
1	9.9e-04	9.09	16736479	175414
2	8.6e-04	51.64	24926999	20594
3	2.3e-04	23.27	23031390	20821
4	1.12e-03	80	27481687	23914
5	4.8e-04	2	9450310	365930
6	6.1e-04	72.91	27227561	22428
7	7.4e-04	30.36	23958962	10900
8	3.5e-04	44.55	24455765	24066
9	1.25e-03	37.45	25369392	14713
10	1.5e-03	16.18	21473494	69879
11	1.0e-04	65.82	23545135	28555
12	3.0e-04	41	24113796	18658
13	2.0e-04	63.29	24176788	26342
14	1.2e-03	7.57	15667597	184512

15	6.0e-04	57.71	25409070	32369
16	1.1e-03	29.86	24546443	29234
17	8.0e-04	13.14	19500926	98851
18	1.0e-04	18.71	20349739	50209
19	7.0e-04	35.43	24691591	12984
20	1.3e-03	68.86	26634371	25827

The Fourth-order Response Surface Function is utilised to fit the dynamic stiffness and damping under various excitation amplitudes and frequencies; afterwards, an approximate function which reflects the relationship between the dynamic stiffness and damping and the excitation amplitudes and frequencies is achieved. Fig.s. 17-18 exhibit a curved surface graph of dynamic stiffness versus amplitude and frequency and a curved surface graph of damping versus amplitude and frequency, respectively. It can be observed from the two Fig.s that the rubber damping ring's dynamic stiffness and damping studied in this research are considerably altered by the excitation frequency, but are rarely affected by the excitation amplitude. The dynamic stiffness of rubber damping ring increases gradually with the escalation of frequency, while the damping decreases as the frequency increases, and the descending rate is slowly decreasing. The prevalence of the results gained in this research is similar to that obtained in references [30][31], which reveals that the stiffness and damping of the rubber damping ring are mainly affected by the excitation frequency when the excitation amplitude is small. In short, the mechanical model constructed in this research achieves excellent precision, efficiency and reliability.

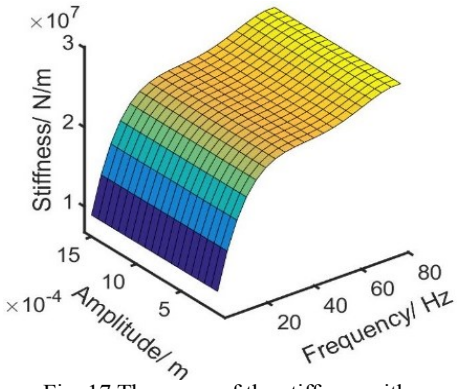

Fig. 17 The curve of the stiffness with excitation amplitude and frequency

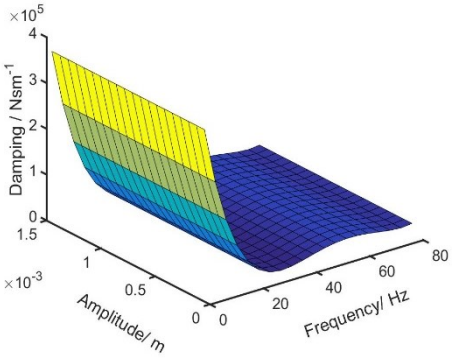

Fig. 18 The curve of the damping with excitation amplitude and frequency

Since the amplitude exerts a small influence on the dynamic characteristics of the rubber damping ring, the mechanical model of the dynamic stiffness and damping can be expressed as follows:

$$\begin{cases} K = a_0 + a_1 F + a_2 F^2 + a_3 F^3 + a_4 F^4 \\ C = b_0 + b_1 F + b_2 F^2 + b_3 F^3 + b_4 F^4 \end{cases} \tag{12}$$

where $a_0 = 6673564.4$, $a_1 = 1478988.837$, $a_2 = -46467.764$, $a_3 = 637.201$, $a_4 = -3.087$; $b_0 = 438609.425$, $b_1 = -38792.117$, $b_2 = 1226.844$, $b_3 = -15.94$, $b_4 = -0.0732$; F represents the excitation frequency.

5 Application and Experimental Verification of Mechanical Model of Rubber Damping Ring in Multi-span Shafting

5.1. Multi-span shafting test platform

Vibration reduction experiments were carried out on multi-span shafting to compare the dynamic response of the rotor system with and without rubber damping ring. The multi-span shafting vibration test platform consists of multi-span shafting, dynamic signal acquisition equipment and a personal computer, as displayed in Fig. 19. The multi-span shafting includes a rotating shaft, an inertia disc, a flexible coupling, fixed support, a motor and the like, in which the supports I and Ⅲare rigid supports, and the support Ⅱ is variable supports, as exhibited in Fig. 20.

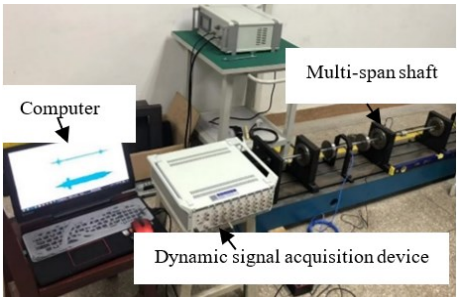

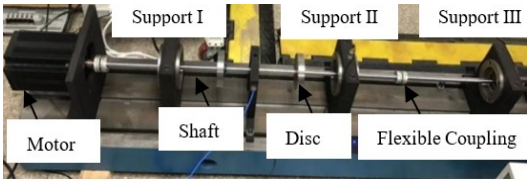

Fig. 19 Multi-span shafting vibration test platform Fig. 20 Multi-span shafting

The test platform employs eddy current sensors to measure the radial displacement of the rotor; meanwhile, an acceleration sensor is placed on the support Ⅱ to measure the radial acceleration. The sensor position is presented in Fig. 21. The internal structure of the support is shown in Fig. 22. The vibration transmission path of the elastic support is sequentially from the shaft, shaft sleeve, ball bearing, bush, rubber damping ring to bearing support. The stiffness of each component is in series relation, so the elastic support's radial stiffness is mainly determined by the rubber damping ring with the smallest rigidity. The internal structure of the rigid support is similar to that of the elastic support, except that the rubber damping ring is replaced by a steel ring; therefore, the radial rigidity is considerably improved.

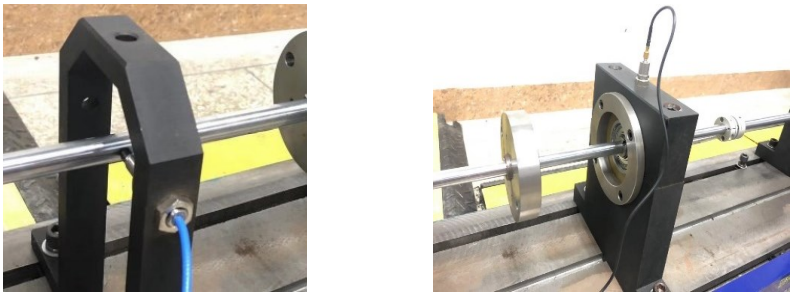

(a) Addy current sensor (b) Acceleration sensor

Fig. 21 Sensor position

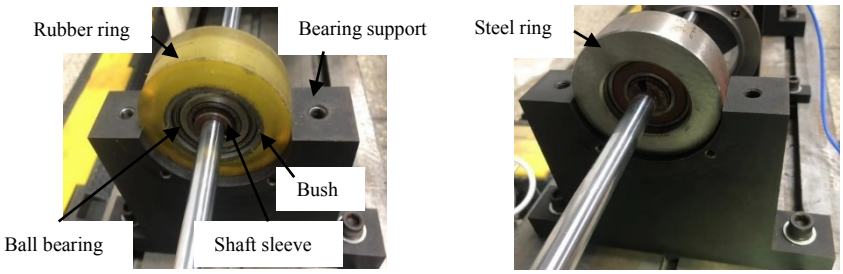

(a) Elastic support (b) Rigid support

Fig. 22 The internal structure of the support

5.2. Dynamic modelling

The multi-span shafting is simplified to facilitate analysis, and its mechanical model is

constructed, as revealed in Fig. 23. The multi-span shafting mechanical model comprises the rotating shaft unit, inertia disc unit, flexible coupling unit, bearing unit, steel ring unit, rubber/steel ring unit and bearing support unit. The rotating shaft is discretised by the beam element, and the nodes of the element are arranged at the bearing support, the disc, the coupling and the like, respectively. Ball bearings take the effects of clearance and time-varying stiffness into account. Bearing supports are connected to the foundation by bolts, assuming their circumferential symmetry. Nodes 1-16 are those corresponding to rotating shaft units, while nodes 17-19 are those corresponding to bearing units, and nodes 20-22 are those corresponding to bearing units. Finally, the finite element method is employed to assemble the element matrices to obtain the overall dynamic equations of the multi-span shafting system.

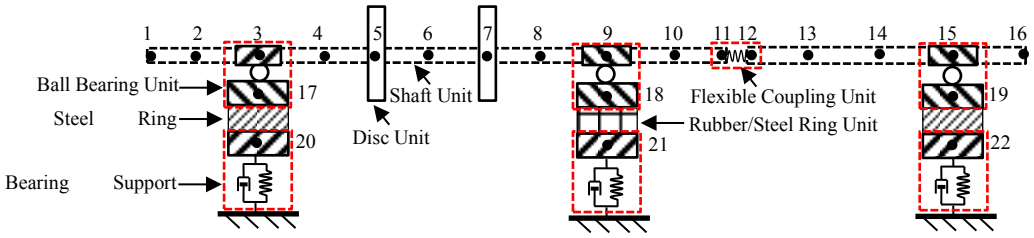

Fig. 23 Mechanical model of multi-span shafting

5.2.1. Dynamic equation of rotating shaft

As illustrated in Fig. 23, the dynamic equation of the rotating shaft needs to consider the influences of the mass and gyro moment of the inertia disk, the flexibility of the coupling and the nonlinear bearing force. Timoshenko beam element with 8 degrees of freedom is employed to establish the finite element model of the rotating shaft. According to existing studies [33-34], mass matrix $\mathbf{M}_e$, stiffness matrix $\mathbf{K}_e$ and gyro matrix $\mathbf{G}_e$ of Timoshenko beam element can be obtained, respectively, as shown in Appendix, in which E and G are elastic modulus and shear modulus, ρ and I stand for density and diametral inertia, A and L denote the element's cross-sectional area and length, σ represents Poisson's ratio, m_L is the shaft element mass, D_i and D_o are the outer and inner diameter of the element. Inertial disk assumes isotropy and merely considers the influence of main directions, where mass matrix $\mathbf{M}_{dk}$ and gyro matrix $\mathbf{G}_{dk}$ are respectively written as follows.

$$M_{dk}=\begin{bmatrix} m_{dk} & & & \\ & m_{dk} & & \\ & & J_{dk} & \\ & & & J_{dk} \end{bmatrix},\quad G_{dk}=\begin{bmatrix} & & & \\ & & & -J_{pk} \\ & & & \\ & & J_{pk} & \end{bmatrix}\quad (k=1,2)$$

Here m_{dk} is the mass of the kth disc; J_{dk} represents the sectional moment of inertia of the kth disk; J_{pk} indicates the polar moment of inertia of the kth disk.

Rotating shafts are generally connected by laminated couplings, which can compensate for axial, angular and radial installation errors. In this research, the finite element analysis of laminated coupling is directly carried out by ANSYS, and the laminated assembly's stiffness matrix can be obtained by

$$K_c = \begin{bmatrix} K_{coupling} & -K_{coupling} \\ -K_{coupling} & K_{coupling} \end{bmatrix}$$

where $K_{coupling} = \begin{bmatrix} k_{cxx} & & & \\ & k_{cyy} & & \\ & & k_{c\theta x} & \\ & & & k_{c\theta y} \end{bmatrix}$, $k_{cxx} = k_{cyy}$ and $k_{c\theta x} = k_{c\theta y}$ represent the radial stiffness and angular stiffness of laminated couplings, respectively, which are illustrated in Table 6.

Table 6 Calculation of Coupling Stiffness

Stiffness	Result
Radial stiffness of coupling (N/m)	9.9×10^8
Angular stiffness of coupling (Nm/rad)	3.98×10^4

Fig. 24 is a schematic structural diagram of a ball bearing, in which N is the number of ball elements of the bearing; ω_φ denotes the angular velocity of the rotor; bearing outer ring radius is R; bearing inner ring radius is r, interference connection with the rotor. According to the kinematic theorem of ball bearing, the ball body's angular velocity ω_{cage} can be obtained as

$$\omega_{cage} = \frac{\omega_\varphi r}{r+R} \tag{13}$$

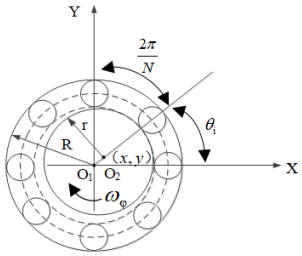

Fig. 24 Schematic diagram of a ball bearing structure

According to the findings of existing studies [35], the nonlinear elastic force $\boldsymbol{F}_{bj}$(j=1,2,3) acting on the rotor can be represented as

$$\boldsymbol{F}_{bj} = \begin{bmatrix} F_{bxj} \\ F_{byj} \end{bmatrix} = \begin{bmatrix} k_p \sum_{i=1}^{N} (w_{\theta_i})^{3/2} \cdot H(w_{\theta_i}) \cdot cos\,\theta_i \\ k_p \sum_{i=1}^{N} (w_{\theta_i})^{3/2} \cdot H(w_{\theta_i}) \cdot sin\,\theta_i \end{bmatrix} \text{ (j=1,2,3)} \tag{14}$$

where F_{bxj} and F_{byj} represent the nonlinear bearing forces of ball bearings in X and Y directions, respectively; $w_{\theta_i} = xcos\theta_i + ysin\theta_i - \gamma_0$, indicating the deformation of the ith ball elements at the angular displacement θ_i; $\theta_i = \omega_{cage}t + \frac{2\pi(i-1)}{N}$, which indicates the angular displacement θ_i of the ith ball element of the bearing at time t; k_p is Hertz contact stiffness; $H(\cdot) = \begin{cases} 1, & \cdot > 0 \\ 0, & \cdot \le 0 \end{cases}$ indicates a function of Haversian.

The beam elements $\mathbf{M}_e$, $\mathbf{K}_e$, $\mathbf{C}_e$ and $\mathbf{G}_e$ of the rotating shaft are assembled based on the finite element theory, and the inertia disk's mass matrix $\mathbf{M}_{dk}$(k = 1,2) and gyro matrix $\mathbf{G}_{dk}$(k=1,2), the laminated coupling's stiffness matrix $\mathbf{K}_c$, and the ball bearing's nonlinear force $\boldsymbol{F}_{bj}$(j=1,2,3) are integrated with the nodes of the corresponding beam elements to obtain the dynamic equations of the rotating shaft, which can be expressed as

$$\mathbf{M}_r\ddot{\mathbf{q}} + (\mathbf{C}_r - \omega\mathbf{G}_r)\dot{\mathbf{q}} + \mathbf{K}_r\mathbf{q} = \mathbf{Q}_r \tag{15}$$

Here $\mathbf{M}_r$ is the overall mass matrix of the rotating shaft, which includes the mass of each beam element and inertia disc; $\mathbf{C}_r$ is the damping matrix of the rotating shaft, i.e. $\mathbf{C}_r = \alpha\mathbf{M}_r + \beta\mathbf{K}_r$; $\mathbf{G}_r$ is the rotating shaft's gyro matrix, including each beam element and inertial disk; $\mathbf{K}_r$ is the stiffness matrix of the rotating shaft, which consists of each beam element and laminated coupling; $\mathbf{Q}_r$ is the external force on the rotating shaft, mainly including unbalanced force and bearing force.

5.2.2. Dynamic equation of bearing outer ring

The outer ring of the bearing is subjected to the bearing force; Simultaneously, it is affected by the authority of the steel ring or the rubber damping ring. Assume that x_{wj} and y_{wj} represent the bearing outer ring's vibration displacement in X and Y directions, respectively, while x_{bj} and y_{bj} indicate the bearing support's vibration displacement in these directions; F_{rxj} and F_{ryj} denote the force of the steel ring or the rubber damping ring on bearing outer ring in X and Y directions, respectively. According to Newton's second law, the differential equations of motion of the bearing's outer ring can be expressed as follows.

$$\begin{cases} m_{bwj}\ddot{x}_{wj} + F_{rxj} = F_{bxj} \\ m_{bwj}\ddot{y}_{wj} + F_{ryj} = F_{byj} \end{cases} \text{(j=1,2,3)} \tag{16}$$

Here: when j=1 or 3, then $\begin{cases} F_{rxj} = K_x(x_{wj} - x_{bj}) + C_x(\dot{x}_{wj} - \dot{x}_{bj}) \\ F_{ryj} = K_y(y_{wj} - y_{bj}) + C_y(\dot{y}_{wj} - \dot{y}_{bj}) \end{cases}$; when j=2 and there is a rubber damping ring between the ball bearing and the bearing support, then $\begin{cases} F_{rxj} = K(x_{wj} - x_{bj}) + C(\dot{x}_{wj} - \dot{x}_{bj}) \\ F_{ryj} = K(y_{wj} - y_{bj}) + C(\dot{y}_{wj} - \dot{y}_{bj}) \end{cases}$; otherwise, $\begin{cases} F_{rxj} = K_x(x_{wj} - x_{bj}) + C_x(\dot{x}_{wj} - \dot{x}_{bj}) \\ F_{ryj} = K_y(y_{wj} - y_{bj}) + C_y(\dot{y}_{wj} - \dot{y}_{bj}) \end{cases}$; in which K_x, K_y, C_x and C_y are the steel ring's stiffness and damping in the X and Y directions, respectively; K and C represent the stiffness and damping of the rubber damping ring, respectively, and are obtained by Equation 11.

5.2.3. Dynamic equation of bearing support

The bearing support is affected by the reaction force of the rubber damping ring or steel ring and the elastic force and damping force between the bearing support and the foundation. Base on Newton's second law, the differential equations of motion of the bearing support can be obtained as follows:

$$\begin{cases} m_{bsj}\ddot{x}_{bj} + k_{\mathrm{xj}}x_{bl} + c_{\mathrm{xj}}\dot{x}_{bl} = F_{rxj} \\ m_{bsj}\ddot{y}_{bj} + k_{\mathrm{yj}}x_{bl} + c_{\mathrm{yj}}\dot{y}_{bl} = F_{ryj} \end{cases} \text{(j=1,2,3)} \tag{17}$$

where m_{bsj} is the mass of the jth bearing support; k_{xj} and k_{yj} represent the stiffness between the jth bearing support and the foundation, respectively; c_{xj} and c_{yj} indicate the damping between the jth bearing support and the foundation, respectively.

5.2.4. Coupling dynamic equation of multi-span shafting

By combining equations (15), (16) and (17), multi-span shafting coupling dynamic equations can be established, as follows:

$$\bar{\mathbf{M}}\ddot{\mathbf{X}} + (\bar{\mathbf{C}} - \omega\bar{\mathbf{G}})\dot{\mathbf{X}} + \bar{\mathbf{K}}\mathbf{X} = \bar{\mathbf{Q}} \tag{18}$$

Here $\bar{\mathbf{M}}$ is the generalised mass matrix of the coupling system; $\bar{\mathbf{C}}$ is the generalised damping matrix of the coupling system; $\bar{\mathbf{G}}$ is the coupling system's generalised gyro matrix; $\bar{\mathbf{K}}$ is the generalised stiffness matrix of the coupling system; $\bar{\mathbf{Q}}$ is the generalised force matrix of the coupled

system

5.3. Solutions and analysis

It can be seen that the coupling dynamic equation of the multi-span shafting is a complex system through the above analysis, and it is difficult to achieve satisfactory results by some existing analytical methods. In this research, Newmark and Newton-Raphson hybrid methods are employed to compute the numerical solution of the system. In order to obtain an accurate dynamic response of the system, the step size is 1/300 of the excitation frequency. The structural parameters of the rotating shaft are exhibited in Table 7, and the rotor is made of steel with a density of 7850 kg/m^3, an elastic modulus of 2.1×10^{11} Pa and a Poisson's ratio of 0.3. The inertial disk's parameters are displayed in Table 8. Relevant parameters of ball bearings are presented in Table 9. Stiffness and damping of the steel ring are displayed in Table 10. The parameters of bearing support are manifested in Table 11.

Table 7 Parameters of shaft

Items	Shaft element						
Node to node	1-2	2-3	3-4	4-5	5-6	6-7	7-8
Outer Diameter/mm	14	14	14	14	14	14	14
Inner Diameter/mm	0	0	0	0	0	0	0
Shaft Length/mm	125	125	75	75	120	120	70
Node to node	8-9	9-10	10-11	12-13	13-14	14-15	15-16
Outer Diameter/mm	14	14	14	14	14	14	14
Inner Diameter/mm	0	0	0	0	0	0	0
Shaft Length/mm	70	95	95	100	110	100	50

Table 8 Parameters of inertial disk

inertial disk	node	Outer Diameter / mm	Inner Diameter / mm	thickness / mm	Density/ kg/m^3
1	5	100	14	20	7850
2	7	100	14	20	7850

Table 9 Parameters of ball bearing

Ball bearing	node	Outer radius/ mm	Inner radius/ mm	Ball number	Contact stiffness/ N/m$^{3/2}$	Gap/ μm	Outer mass/ kg
1	17	52	25	13	7.055×10^9	10	0.5
2	18	52	25	13	7.055×10^9	10	0.5
3	19	52	25	13	7.055×10^9	10	0.5

Table 10 Parameters of steel ring

Steel ring	k_x/ N/m	c_x/ N·s/m	k_y/ N/m	c_y/ N·s/m
1	6×10^8	500	6×10^8	500
2	6×10^8	500	6×10^8	500

3	6×10^8	500	6×10^8	500

Table 11 Parameters of bearing supporting

Bearing support	node	k_x/ N/m	c_x/ N·s/m	k_y/ N/m	c_y/ N·s/m	Mass/ kg
1	20	2×10^8	1000	2×10^8	1000	8
2	21	2×10^8	1000	2×10^8	1000	8
3	22	2×10^8	1000	2×10^8	1000	8

5.3.1. Verification of dynamic model of multi-span shafting

The inertial disk exists an unbalance amount due to material and manufacturing errors. A unbalance value is applied to the disk node 5 of the multi-span shafting dynamic model. Subsequently, the results of the test and theoretical analysis are compared, which provides a theoretical basis for subsequent verification of the precision of the rubber damping ring mechanical model.

The multi-span shafting dynamic model without rubber damping ring is investigated numerically and experimentally. Fig. 25 is a comparative analysis of experimental and theoretical results of the accelerated motion of multi-span shafting. The test results exhibit that the first-order rotation speed of the multi-span shafting experiment platform is 3360r/min, and the corresponding displacement amplitude is 7.2×10^{-4}m. The first-order critical speed obtained by solving the dynamic model is 3171r/min, and its magnitude is 6.8×10^{-4}m. The average error rate between them is less than 10%. The above study proves that the multi-span shafting dynamic model established in this research holds superior accuracy and can be utilised to predict the real-world multi-span shafting's dynamic characteristics.

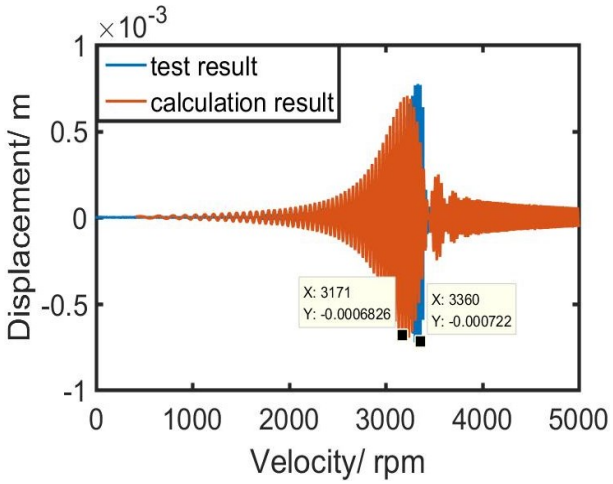

Fig. 25 Vibration displacement of accelerated motion of the test and theoretical analysis

5.3.2. Vibration reduction analysis of multi-span shafting by rubber damping ring

(1) Response analysis of the accelerated motion of the rotating shaft

The rotating shaft is accelerated with an angular acceleration of $\alpha = 155\text{rad/s}^2$ through the control of the variable-frequency motor, and then keeps the rotational speed constantly after reaching the speed of 5000r/min. The response of accelerated motion of the rotating shaft with and without the rubber damping ring is experimented, respectively, as presented in Fig. 26. It can be known from the test that when the rubber damping ring is installed at the support II, the system's first-order natural frequency declines due to the reduction of the overall stiffness of the

multi-span shafting; meanwhile, the amplitude of the vibration is obviously reduced at the critical point due to the damping influence of the rubber damping ring, which is favourable for the multi-span shafting to smoothly cross the critical point and improve the service life of the system.

Fig. 27 is the acceleration vibration response of the rotating shaft with and without rubber damping rings obtained by the theoretical solution. The natural frequency of the system will deteriorate when the system's support contains a rubber damping ring, and the vibration amplitude will reduce significantly at the critical speed, which is similar to the test results. The experiment and theoretical solutions of the vibration reduction ratio are compared at the critical point, which can be observed that the vibration reduction ratio of the test is 44%, and that obtained by the simulation is 38%; therefore, the error between the two is 13.6%.

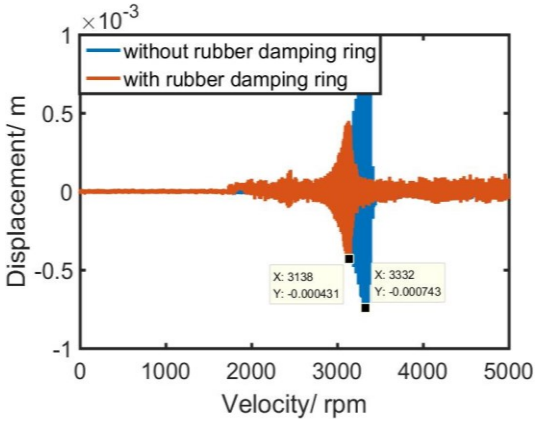

Fig. 26 Accelerated motion experiment of the rotating shaft with or without rubber damping ring

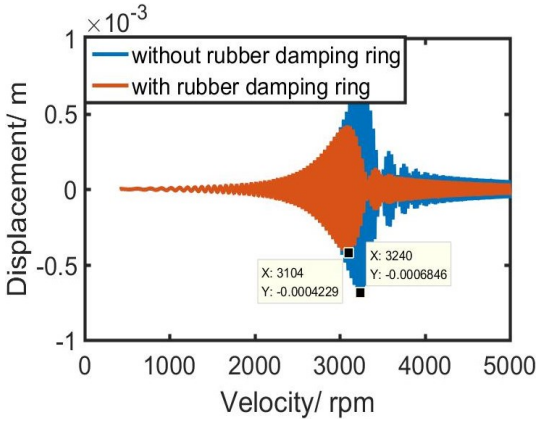

Fig. 27 Accelerated motion simulation of rotating shaft with or without rubber damping ring

(2) Steady-state response analysis

The acceleration response at support II with or without rubber damping ring was measured via experiments under the rotating speeds of $n = 2000\mathrm{r/min}$ and $n = 4000\mathrm{r/min}$, as exhibited in Fig. 28. Moreover, Fig. 29 illustrates the acceleration response of the rotating shaft with or without a rubber damping ring obtained by the theoretical solution at various rotating speeds. The comparison of the test and simulation results reveal that the error of the vibration reduction rate of rubber damping ring is less than 17% at different rotating speeds, as shown in Table 12. In short, our research can provide useful theoretical guidance pertaining to the engineering design of the rubber damping ring.

Table 12 Comparative analysis of vibration reduction rates of test and simulation at the different rotational speed

Speed	Vibration reduction ratio		Error
	Test	Simulation	
2000r/min	42%	37.2%	16.6%
4000r/min	49%	41%	16.3%

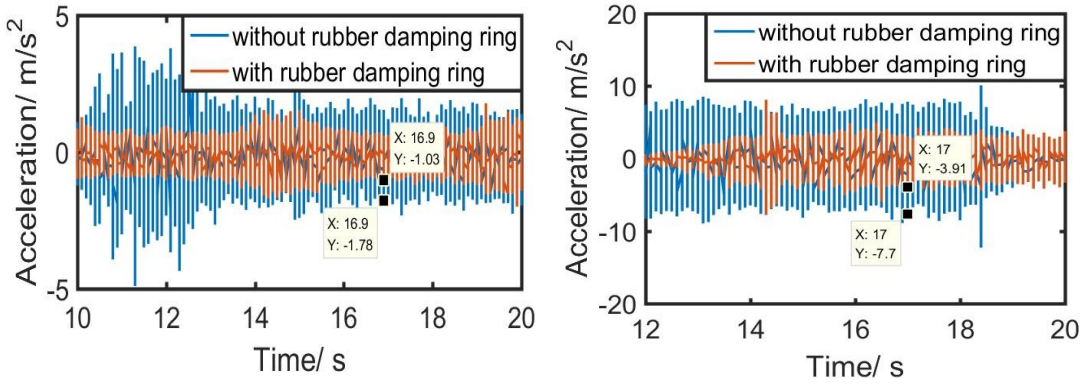

(a) $n = 2000\mathrm{r/min}$ (b) $n = 4000\mathrm{r/min}$

Fig. 28 Test results at a different speed

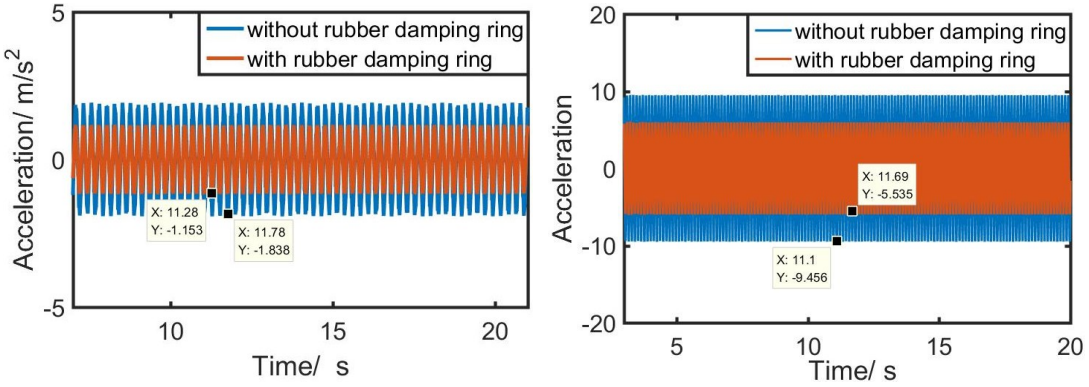

(a) $n = 2000\mathrm{r/min}$ (b) $n = 4000\mathrm{r/min}$

Fig. 29 Theoretical analysis results at a different speed

6 Conclusions

In this research, a mechanical model of rubber damping ring is established by means of experiments, parameter separation methods and joint simulations. The mechanical model of a rubber damping ring is applied to the vibration reduction analysis of multi-span shafting, and the following conclusions are obtained:

(1) The constitutive model parameters of hyperelasticity and viscoelasticity of the rubber material are identified by joint simulation. Subsequently, it verified experimentally. It can be observed that the hysteresis loops acquired by simulation and experiment are basically in coincidence; meanwhile, the maximum error rate of dynamic stiffness and damping obtained by experiment and simulation is not more than 7%.

(2) Based on the experimental design and approximate model method in the joint simulation platform, the mechanical model of the dynamic stiffness and the damping of rubber damping ring are proposed. Due to taking the working states into account, the dynamic stiffness and damping of the rubber damping ring are mainly influenced by the excitation frequency, while the vibration amplitude exerts an insignificant impact. The obtained mechanical model is a function of excitation frequency and can be conveniently coupled with the dynamic rotor system for dynamic analysis.

(3) The dynamic equations of multi-span shafting with and without rubber damping ring are established by the finite element and lumped mass method. On this basis, the vibration reduction analysis of rubber damping ring is carried out. The experimental results exhibit that the theoretical and experimental error of vibration reduction rate is less than 17%, which indicates that the

mechanical model of the rubber damping ring established in this research has superior precision and reliability.

The research provides a new idea for establishing the mechanical model of the rubber damping ring. However, the influence of special working conditions such as temperature on the dynamic characteristics of the rubber damping ring is not considered. In the future, a mechanical model of the rubber damping ring considering the effect of temperature will be further established.

Data Availability

The data used to support the findings of this study are included within the article.

Declaration of Conflicting Interests

The author(s) declared no potential conflicts of interest with respect to the research, authorship, and/or publication of this article.

Acknowledgements

This research is supported by the National Natural Science Foundation of China (Nos. 51775277 and 51775265) and NUAA Short Visiting Program (Grant no. 190624DF01).

References

[1] Singh M P, Moreschi L M (2002) Optimal placement of dampers for passive response control. Earthquake Eng Struct Dyn. 31: 955-976.

[2] Shukla A K, Datta T K (1999) Optimal use of viscoelastic dampers in building frames for seismic force. J Struct Eng. 125: 401-409.

[3] Singh M P, Chang T S (2009) Seismic analysis of structures with viscoelastic dampers. J Eng Mech. 135: 571-580.

[4] Miehe C, Keck J (2000) Superimposed finite elastic–viscoelastic–plastoelastic stress response with damage in filled rubbery polymers. Experiments, modelling and algorithmic implementation. J Mech Phys Solids. 48(2): 323-365.

[5] Chang TS, Singh MP (2009) Mechanical model parameters for viscoelastic dampers. J Eng Mech. 135: 581-584.

[6] Palmeri A, Ricciardelli F, De Luca A, Muscolino G (2003) State space formulation for linear viscoelastic dynamic systems with memory. J Eng Mech. 129(7): 715-724.

[7] Park S W (2001) Analytical modeling of viscoelastic dampers for structural and vibration control. Int J Solids Struct. 38: 8065-8092.

[8] Sjöberg M, Karl L (2002) Non-linear behavior of a rubber isolator system using fractional derivatives. Vehicle Syst Dyn. 37: 217-236.

[9] Sjöberg M (2003) Nonlinear isolator dynamics at finite deformations: An effective hyperelastic, fractional derivative, generalized friction model. Nonlinear Dynam. 33: 323-336.

[10] Berg M (1998) A non-linear rubber spring model for rail vehicle dynamics analysis. Vehicle Syst Dyn. 30: 197-212.

[11] Hill J M (1975) Radial deflections of rubber bush mountings of finite lengths. Int J Eng Sci, 13: 407-422.

[12] Luo R K, Wu W D, Xu Q G, et al (2017) An energy dissipation approach on complete loading-unloading and dynamic impact predictions with experimental verification for rubber

anti-vibration component. Polym Test, 63: 314-322.
[13] Zhao R G, Xu Y J, Chen Z F, et al (2004) New dynamics model for nonlinear hysteresis vibration isolation system. Chinese Journal of Mechanical Engineering. 40(2): 185-188.
[14] Yu Z J, Zhang L J, Yu Z P (2010) Semi-empirical parameterized dynamic model of rubber bushing mechanical properties. Chinese Journal of Mechanical Engineering. 46(14): 115-123.
[15] Zhao G, Liu J, Liu Z S (2010) Theoretical and experimental study on nonlinear dynamic model of a rubber isolator. Journal of Vibration and Shock. 29(1): 173-177.
[16] Hartmann S, Tschope T, Schreiber L, et al (2003) Finite deformations of a carbon black-filled rubber. Experiment, optical measurement and material parameter identification using finite elements. Eur J Mech A-Solid. 22(3): 309-324.
[17] Wang L R, Lu Z H (2003) Modeling method of constitutive law of rubber hyperelasticity based on finite element simulations. Rubber Chem Technol. 76(1): 271-285.
[18] Sasso M, Palmieria G, Chiappinia G, et al (2008) Characterization of hyperelastic rubber-like materials by biaxial and uniaxial stretching tests based on optical methods. Polym Test. 27(8): 995-1004.
[19] Meunier L, Chagnon G, Favier D, et al (2008) Mechanical experimental characterization and numerical modeling of an unfilled silicone rubber [J]. Polym Test. 27(6): 765-777.
[20] Charlton D J, Yang J, Teh K K (1994) A review of methods to characterize rubber elastic behavior for use in finite element analysis. Rubber Chem Technol. 67(3): 487-503.
[21] Zielnica J, Ziolkowski A, Cempel C (2003) Non-linear vibroisolation pads design, numerical FEM analysis and introductory experimental investigations. Mech Syst Signal Process 17(2): 409-422.
[22] Negrete N G, Vinolas J, Kari L (2006) A simplified methodology to predict the dynamic stiffness of carbon-black filled rubber isolators using a finite element code. J Sound Vib. 296: 757-776.
[23] Rahnavard R, Thomas R J (2019) Numerical evaluation of steel-rubber isolator with single and multiple rubber cores. Eng Struct. 198, 1-15.
[24] Sheikhi J, Fathi M, Rahnavard R (2020). Natural rubber bearing incorporated with high toughness steel ring dampers. Structures 24: 107-123.
[25] Liu W W, Weng X T, Zhu S J, et al (2007) Study on a new method to identify parameters of strain-energy density function of a rubber. Journal of Vibration and Shock. 26(7): 1-10.
[26] Liu W W, Weng X T, Zhu S J, et al (2010) Study on anti-optimization method to identify the parameters of viscoelastic model of rubber. Journal of Vibration and Shock. 29(8): 185-188.
[27] Gil-Negrete N, Viñolas J, Kari L (2006) A simplified methodology to predict the dynamic stiffness of carbon-black filled rubber isolators using a finite element code. J Sound Vib. 296: 757-776.
[28] Mordini A, Strauss A (2008) An innovative earthquake isolation system using fibre reinforced rubber bearings. Eng Struct. 30: 2739-2751.
[29] Sun D W, Zhang G Y (2010) A new approach to identify hysteretic damping of a rubber isolator. Journal of Vibration and Shock. 29(4): 164-168.
[30] Sun D W, Chen Z G, Zhang G Y, et al (2011) Modeling and parameter identification of amplitude- and frequency-dependent rubber isolator. J Cent South Univ Technol. 18: 672−678.
[31] Han D B, Song X G (2009) Experimental study on constitutive model for damping and stiffness of a rubber isolator. Journal of Vibration and Shock. 28(1): 156-160+203.

[32] Ambrisko L, Marasova D, Cehlar M (2017) Investigating the tension load of rubber composites by impact dynamic testing. Bull Mater Sci. 40(2): 281-287.
[33] Hutchinson J R (2001) Shear coefficients for Timoshenko beam theory, J Appl Mech-T ASME, 68: 959-960.
[34] Friswell M I, Penny J E T, Garvey S D, et al (2010) Dynamics of rotating machines, Cambridge University Press, London.
[35] Harris T A (2003) Rolling bearing analysis, John Wiley & Sons, New York.

Appendix

$$\mathbf{M}_e = \begin{bmatrix} m1 & 0 & 0 & m2 & m3 & 0 & 0 & m4 \\ 0 & m1 & -m2 & 0 & 0 & m3 & -m4 & 0 \\ 0 & -m2 & m5 & 0 & 0 & m4 & m6 & 0 \\ m2 & 0 & 0 & m5 & -m4 & 0 & 0 & m6 \\ m3 & 0 & 0 & -m4 & m1 & 0 & 0 & -m2 \\ 0 & m3 & m4 & 0 & 0 & m1 & m2 & 0 \\ 0 & -m4 & m6 & 0 & 0 & m2 & m5 & 0 \\ m4 & 0 & 0 & m6 & -m2 & 0 & 0 & m5 \end{bmatrix}$$

where

$m1 = 312 + 588\phi + 280\phi^2$; $m2 = (44 + 77\phi + 35\phi^2)\ L$; $m3 = 108 + 252\phi + 140\phi^2$;

$m4 = -(26 + 63\phi + 35\phi^2)L$; $m5 = (8 + 14\phi + 7\phi^2)\ L^2$; $m6 = -(6 + 14\phi + 7\phi^2)L^2$;

$$\phi = \frac{12EI}{G\lambda L^2};\quad \lambda = \frac{6(1+\sigma)^2(1+(\frac{D_i}{D_o})^2)^2}{(7+12\sigma+4\sigma^2)(1+(1+(\frac{D_i}{D_o})^2)^2+4(\frac{D_i}{D_o})^2(5+6\sigma+2\sigma^2)}.$$

$$\mathbf{K}_e = \frac{EI}{(1+\phi)L^2}\begin{bmatrix} 12 & 0 & 0 & 6L & -12 & 0 & 0 & 6L \\ 0 & 12 & -6L & 0 & 0 & -12 & -6L & 0 \\ 0 & -6L & (4+\phi)L^2 & 0 & 0 & 6L & (2-\phi)L^2 & 0 \\ 6L & 0 & 0 & (4+\phi)L^2 & -6L & 0 & 0 & (2-\phi)L^2 \\ -12 & 0 & 0 & -6L & 12 & 0 & 0 & -6L \\ 0 & -12 & 6L & 0 & 0 & 12 & 6L & 0 \\ 0 & -6L & (2-\phi)L^2 & 0 & 0 & 6L & (4+\phi)L^2 & 0 \\ 6L & 0 & 0 & (2-\phi)L^2 & -6L & 0 & 0 & (4+\phi)L^2 \end{bmatrix}$$

$$\mathbf{G}_e = \frac{\rho I}{15L(1+\phi)^2}\begin{bmatrix} 0 & -g1 & g2 & 0 & 0 & g1 & g2 & 0 \\ g1 & 0 & 0 & g2 & -g1 & 0 & 0 & g2 \\ -g2 & 0 & 0 & -g3 & g2 & 0 & 0 & -g4 \\ 0 & -g2 & g3 & 0 & 0 & g2 & g4 & 0 \\ 0 & g1 & -g2 & 0 & 0 & -g1 & -g2 & 0 \\ -g1 & 0 & 0 & -g2 & g1 & 0 & 0 & -g2 \\ -g2 & 0 & 0 & -g4 & g2 & 0 & 0 & -g3 \\ 0 & -g2 & g4 & 0 & 0 & g2 & g3 & 0 \end{bmatrix}$$

where

$g1 = 36$; $g2 = (3 - 15\phi)L$; $g3 = (4 + 5\phi + 10\phi^2)L^2$; $g4 = (-1 - 5\phi + 5\phi^2)L^2$.